applied sciences

MDPI

Article

Copper/Nickel-Decorated Olive Pit Biochar: One Pot Solid State Synthesis for Environmental Remediation

Ahmed M. Khalil [1,2,*], Laurent Michely [2], Rémy Pires [2], Stéphane Bastide [2,*], Khouloud Jlassi [3], Souad Ammar [4], Mohamed Jaziri [5] and Mohamed M. Chehimi [2,4,*]

1 Photochemistry Department, National Research Centre, Dokki, Giza 12622, Egypt
2 Université Paris Est, CNRS, ICMPE (UMR 7182), 94320 Thiais, France; michely@icmpe.cnrs.fr (L.M.); pires@icmpe.cnrs.fr (R.P.)
3 Center for Advanced Materials, Qatar University, Doha P.O. Box 2713, Qatar; khouloud.jlassi@qu.edu.qa
4 Université de Paris, CNRS, ITODYS (UMR 7086), 75013 Paris, France; ammarmer@univ-paris-diderot.fr
5 Laboratoire Electrochimie et Environnement, Ecole Nationale d'Ingénieurs de Sfax, Université de Sfax, Sfax 3038, Tunisia; mohamed.jaziri@enis.tn
* Correspondence: akhalil75@yahoo.com (A.M.K.); bastide@icmpe.cnrs.fr (S.B.); mmchehimi@yahoo.fr (M.M.C.)

Featured Application: Valorization of agrowaste biochar into catalytic material for environmental remediation potential application.

Abstract: Developing micro- and nanomaterials for environmental pollution remediation is currently a pertinent topic. Among the plethora of strategies, designing supported nanocatalysts for the degradation of pollutants has achieved prominence. In this context, we are addressing one of the UN Sustainable Development Goals by valorizing agrowaste as a source of biochar, which serves as a support for bimetallic nanocatalysts. Herein, olive pit powder particles were impregnated with copper and nickel nitrates and pyrolyzed at 400 °C. The resulting material consists of bimetallic CuNi-decorated biochar. CuNi nanocatalysts were found to be as small as 10 nm and very well dispersed over biochar with zero valent copper and nickel and the formation of copper–nickel solid solutions. The biochar@CuNi (B@CuNi) exhibited typical soft ferromagnet hysteresis loops with zero remanence and zero coercivity. The biochar@CuNi was found to be an efficient catalyst of the reduction in methyl orange (MO) dye, taken as a model pollutant. In sum, the one-pot method devised in this work provides unique CuNi-decorated biochar and broadens the horizons of the emerging topic of biochar-supported nanocatalysts.

Keywords: agrowaste valorization; olive pit; Biochar; CuNi bimetallic nanocatalyst; methyl orange; clean water and sanitation

Citation: Khalil, A.M.; Michely, L.; Pires, R.; Bastide, S.; Jlassi, K.; Ammar, S.; Jaziri, M.; Chehimi, M.M. Copper/Nickel-Decorated Olive Pit Biochar: One Pot Solid State Synthesis for Environmental Remediation. *Appl. Sci.* **2021**, *11*, 8513. https://doi.org/10.3390/app11188513

Academic Editor: Rafael López Núñez

Received: 12 August 2021
Accepted: 7 September 2021
Published: 14 September 2021

1. Introduction

Recently, the materials science community witnessed a sky-rocketing number of research papers on biochar. A search on Web of Science with the keyword "biochar" returned the following results: 2 papers in 2001, 221 in 2011, 1413 in 2016, 4333 in 2020 and 3238 in 2021 (accessed on 12 August 2021), which means that over 5000 papers should be published on the topic by the end of 2021. This attests to the vitality of this branch of materials science.

The rationale for the rush in research on biochar lies in the availability of biomass worldwide in different forms, such as agrowastes, i.e., peels [1], leaves [2], palm fronds [3] and seeds [4]. The production of biochar depends on various parameters: the initial composition of the biomass [5] and the pyrolysis parameters [6]. Biochar production falls within the energy sector as it yields bio-oil and biogas in addition to the biochar itself. Biochar is employed in agriculture for soil remediation and as an adsorbent in

environmental applications, e.g., the removal of organic and inorganic pollutants. In the domain of materials science, biochar was found to be a unique source for making graphene [7] but raised hope, if valorized, for its use as a support of nanocatalysts [8]. In the latter case, biochar is usually produced then post-treated for the immobilization of metal ions, which is followed by in situ reduction, resulting in immobilized nanocatalysts [9]. For other purposes, metal ions are loaded on the biochar (or other carbon allotrope) and calcined to provide immobilized metal oxide nanocatalysts [10].

In order to reduce the steps needed to create biochar-immobilized nanocatalysts, we reasoned that the initial biomass could be loaded with metal ions and the modified biomass powder could be pyrolyzed in view of obtaining, in one step, nanocatalysts-coated biochar. This approach is attractive and has seldom been reported; it involves the design of rice husk biochar-immobilized copper metallic nanocatalysts for the catalytic cracking of biomass primary tar [11]. As an alternative method, hydrothermal carbonization may prepare hydrochar-immobilized copper nanoparticles in a single step, but this requires a long process time and additional $NaBH_4$ to reduce the metal ions [12]. Carbothermal production is another process that is mostly employed for recycling used batteries [13], although it has recently also been extended to designing carbon-loaded catalysts [14]. Olive stones are also widely valorized agrowastes, e.g., as biofillers for polymer composites [15,16]. In 2017, olive stone powders were used as biosourced cellulosic supports of silver and gold nanoparticles, and the final olive pit-supported nanocatalysts facilitated the degradation of para-nitrophenol [17]. Herein, we take the advantage of this widely available agrowaste from Tunisia (a country in the top five producers of olive oil by volume [18]) to make nanocatalyst-decorated biochar. Instead of the noble metals, silver and gold, we instead targeted copper–nickel bimetallic nanocatalysts. These supported bimetallic nanoparticles served as electrocatalysts for the reduction of nitrates in wastewater [19] and as heterogeneous catalysts for the reduction of dyes [20].

Herein, we bridge the gap between the use of olive pit powder particles as a support of noble nanocatalysts and the unique, single-step making of biochar-immobilized low-cost bimetallic copper–nickel nanocatalyst. The final copper–nickel-decorated olive pit biochar hybrid was characterized in terms of its morphology, elemental and chemical composition, crystalline structure, thermal stability and response to a magnetic field. It was then tested as a potential heterogeneous catalyst of the discoloration of Methyl Orange aqueous solution. As it stands, this work fulfils three requirements: (i) the valorization of agrowaste as biochar, (ii) biochar-supported nanocatalysts for dye degradation application, and (iii) tackling one of the United Nations' Sustainable Development Goals pertaining to environmental remediation and the production of clean water.

2. Materials and Methods

2.1. Materials

Olive pit (OP) solid waste is an industrial by-product of the olive oil extraction process from Tunisia. The remaining olive oil was further treated with hexane, and the remaining solid olive waste was dried to evaporate water. The resulting residue was cryo-ground to fine particles (in the 60–400 μm range) [15]. The OPs employed in this work contain fat and wax: 10; pectine: 6.6; lignin: 16; hemicellulose: 43; ash: 2; and cellulose: 22.4 wt.% as determined by French Standard method NFT12-011 (equivalent to ISO 638). $Cu(NO_3)_2{\cdot}3H_2O$ and $Ni(NO_3)_2{\cdot}6H_2O$ were purchased from Aldrich and used as received.

2.2. Preparation of Metallic Nanoparticle-Coated Biochar

Weighed olive pit particles were added to metallic salt solutions via stirring. The mixtures were stirred at RT for 30 min and then poured over a glass lens and left to dry overnight. Due to the very hydrophobic nature of olive pit particles [17], the metal–salt solutions were prepared using ethanol as a solvent.

The olive pit and metal ion salt mixtures were weighed again, and, when steady-state mass was noticed, they were subjected to pyrolysis in a tube furnace (Thermolyne, model 21100) under a nitrogen–hydrogen mixture (95/5%). Table 1 reports the experimental conditions.

Table 1. Biochar loads and weights with copper and nickel: from the olive pit (OP) to the CuNi-decorated biochar, including pyrolysis conditions.

Materials	OP Mass (g)	$Cu(NO_3)_2{\cdot}3H_2O$ Mass (g)/mmol	$Ni(NO_3)_2{\cdot}6H_2O$ Mass (g)/mmol	Solvent (mL)	Pyrolyzed OP + Metal Ion Mixture (g)	Biochar Mass (g) and Yield (%)	Expected, Final Metal/Biochar Ratio (mmole/g)
Pyrolysis conditions: 30 °C/min; T_{max}: 400 °C; Dwell time: 15 min							
B	-	-	-	-	0.515	0.136 (26.4%)	0
B@CuNi	3.670	0.843/3.489	1.007/3.463	Ethanol, 10	0.775	0.169 (21.9%)	5.521 mmol/g
B@Cu	3.674	0.849/3.514	-	Ethanol, 10	1.192	0.372 (31.2%)	2.489 mmol/g
B@Ni	3.67	-	1.012/3.480	Ethanol, 10	1.288	0.367 (28.5%)	2.608 mmol/g

2.2.1. Materials Characterization

SEM images and EDX spectra were acquired using a Zeiss Merlin Field Emission Scanning Electron Microscope operating at 5 kV (Oberkochen, Germany) coupled with a SDD X-Max from Oxford Instruments. In order to avoid static charge on the surface, all samples were coated with a 3 nm-thin layer of palladium using a Cressington 208HR sputter-coater coupled with a Cressington MTM-20 thickness controller.

TGA measurements were performed with a Setaram apparatus (Setsys Evolution model). The ramp was from RT to 800 °C at a 10 °C/min heat rate.

The XRD patterns of all of the prepared samples were recorded using X'Pert-Pro Panalytical diffractometer equipped with a Cobalt X-ray source (λ = 1.7889 Å) and operating in the reflexion Bragg–Brentano geometry.

Magnetic measurements were conducted at room temperature on a Vibrating Sample Magnetometer (VSM) from QUANTUM DESIGN.

The biochar sample was characterized using a Horiba HR 800 apparatus fitted with a He−Ne laser beam, the wavelength of which was set at 514 nm.

2.2.2. Catalysis Assays

The catalytic reduction of methyl orange was conducted in the following conditions. In a quartz cuvette 1 cm in length, 4 mL of 20 ppm Methyl Orange solution was incubated with 1 mg of B@CuNi. The mixture was sonicated in a water bath for 2 min, then 30 mg of $NaBH_4$ was added to proceed with the catalysed discoloration reaction. The UV-vis spectra were recorded using a Varian Cary 50 Bio apparatus.

3. Results

3.1. General Strategy of the Work

Several methods of making biochar from various sources have recently been summarized [6].The route for biochar is depicted in Figure 1a (upper panel): olive pit powder is the source of biomass, pyrolysis is the type of treatment and biochar stands for the main product. Slow and mild pyrolysis conditions were adopted: 30 °C/min heating under a nitrogen/H_2 (5%) atmosphere with a dwell time of 15 min at 400 °C prior to cooling at room temperature (RT). A temperature of 400 °C ensures a maximal biochar yield, whilst H_2 was employed in order to ensure metal ion reduction to the metallic state. The lower panel of Figure 1 displays the digital photographs of olive pit powder (Figure 1b), the same powder impregnated with the copper and nickel nitrates mixture (Figure 1c), olive pit biochar (Figure 1d) and biochar-supported CuNi nanoparticles (Figure 1e).

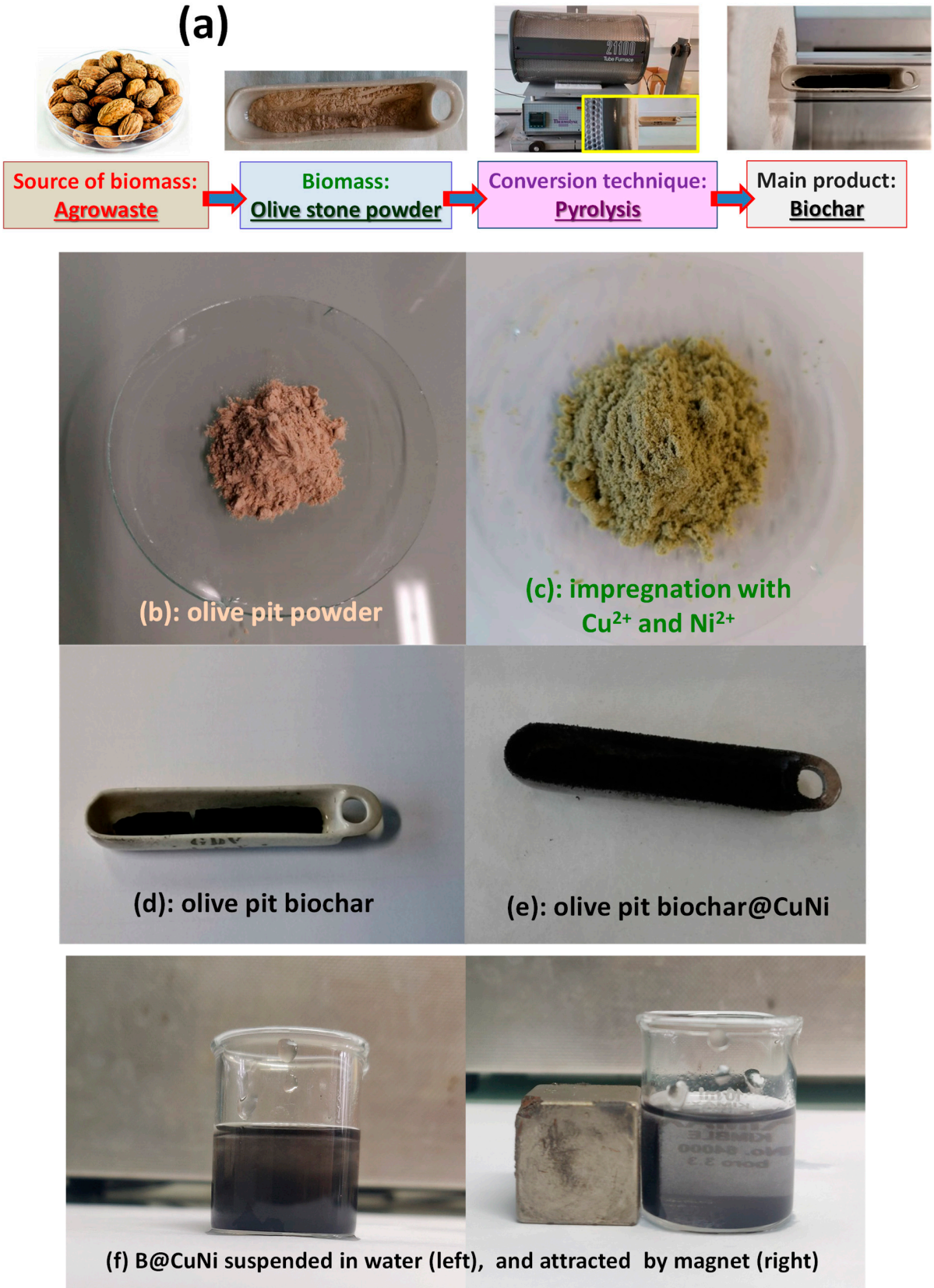

Figure 1. (**a**) Upper panel showing route for making biochar from olive pit biochar. Middle panel shows digital photographs of (**b**) olive pit powder, (**c**) olive pit powder after impregnation into copper and nickel nitrates, (**d**) the olive pit biochar, and (**e**) CuNi-decorated biochar obtained by direct pyrolysis of powder shown in (**c**). Lower panel: (**f**) digital pictures showing suspension of B@CuNi before (**left**) and after attraction by a magnet (**right**).

It is interesting to note that, due to the nickel, the copper–nickel alloy-decorated biochar (B@CuNi) is magnetic and could be attracted by a magnet (Figure 1f, and Video S1, also available at https://vimeo.com/563456328, accessed on 10 September 2021).

3.2. Surface Morphology and Elemental Analysis

Figure 2 displays SEM images of pristine and decorated biochar samples. Figure 2a depicts the surface morphology of CuNi-decorated biochar. It shows a porous, extending surface area for the nanocatalyst-decorated biochar. CuNi nanoparticles are spread along the top of the carbonaceous sample. Upon magnifying the SEM image to provide more comprehensive information, a clearer distribution of the metallic nanoparticles can be observed, as shown in Figure 2b. It is advantageous to notice CuNi nanoparticles covering the inner surface of the pores of biochar in the form of light spots on the inner denser surface surrounded by a circle and ellipse in Figure 2b. CuNi nanoparticles appear as distinct spheres, avoiding any aggregates that may arise in such cases, as illustrated in the inset of Figure 2c. They provide a spherical, undeformed structure for the provided nanoparticles. Upon comparing the B@CuNi surface to that of the pristine biochar, fewer pores can be visualized on the surface, as displayed in Figure 2d. These pores evidently manifest at higher magnification, as illustrated in Figure 2e, in a smaller proportion when compared to the CuNi-biochar sample. The inset in Figure 2f is mentioned here as a reference sample in the absence of the CuNi-supporting catalyst. The bare biochar micrograph denotes a plain surface without much informative morphology, and its porous structure cannot be easily recognized.

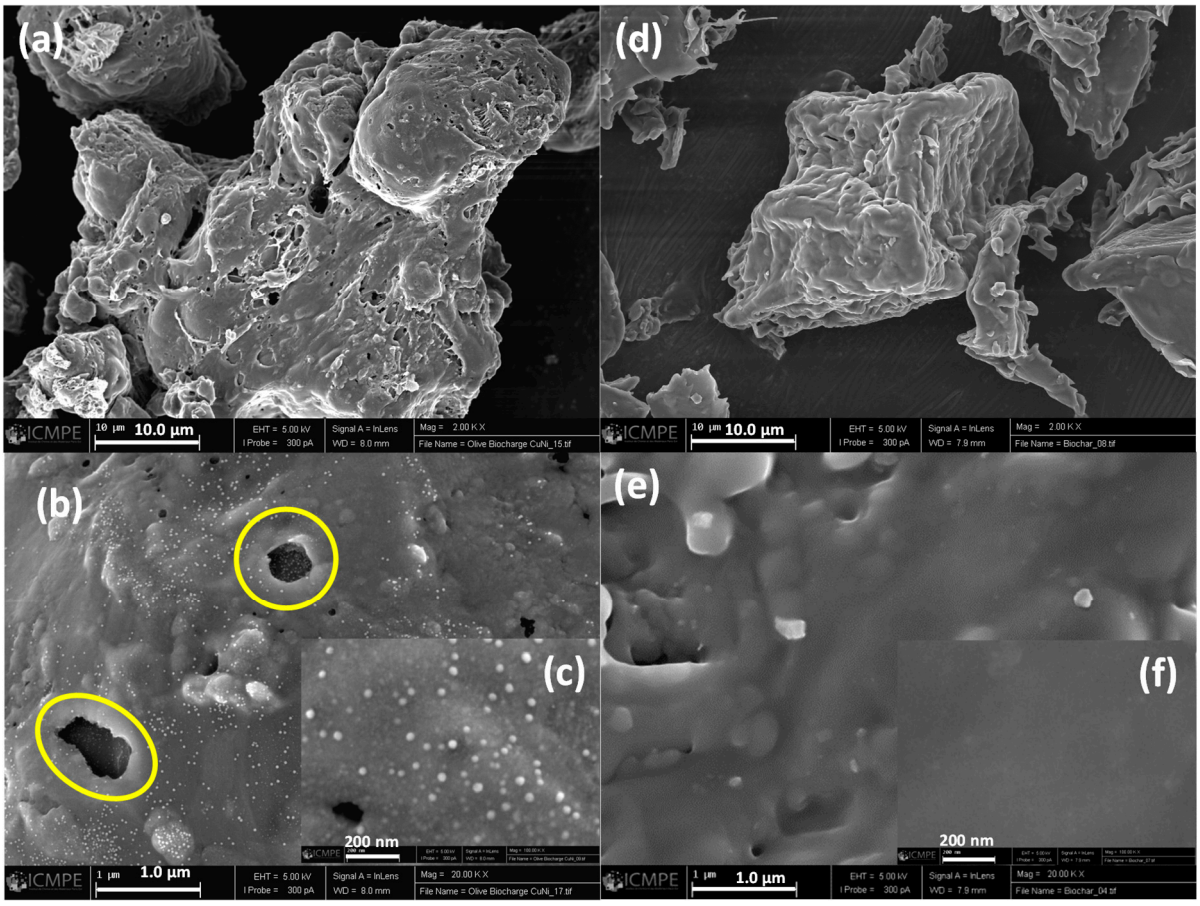

Figure 2. SEM images of biochar/CuNi hybrid (**a**–**c**) and the reference pristine biochar (**d**–**f**) without any supported nanocatalysts, at indicated magnifications. Some pores (in (**b**)) enriched with CuNi nanoparticles are surrounded by a circle and an ellipse.

EDX was used to determine the surface composition of B@CuNi over several spots. For comparison, we have also recorded EDX spectra for OP impregnated with metal salts, and the bare OPs. Figure 3a–c display the EDX spectra of the OPs, OP@metal salts and B@CuNi. The elemental composition of B@CuNi is displayed in Figure 3d, whereas the atomic ratios of (Cu+Ni)/(C+O) and Cu/Ni are compared in Figure 3e for OP@metal salts and B@CuNi. Figure 3a–c conclusively demonstrate the absence of any copper and nickel ions from the surface of the OPs, whereas the characteristic Cu and Ni peaks are noted on the impregnated OP particles with peak intensity increasing in the order Cu~Ni < O < C. The increase in the O/C peak intensity ratio is due to the hydrated metal nitrates. Upon pyrolysis, the metal nitrate-impregnated OPs are transformed into metallic alloy-decorated biochar B@CuNi with relative peak intensity increasing in the order O < Cu~Ni < C. Quantitatively, Figure 3d displays the C, O, Cu and Ni atomic % at 15 spots from the B@CuNi powder sample; the composition is fairly similar from one spot to another, which indicates even decoration of the biochar with metallic nanoparticles. This is due to homogenous impregnation of the OPs with metal nitrates. The (Cu+Ni)/(C+O) atomic ratio (Figure 3d) increases continuously from OP@metal salts to B@CuNi due to the pyrolysis of the olive stones and subsequent release of water and nitrates. Figure 3e shows that the Cu/Ni atomic ratio remains the same within the standard deviation for OP@metal salts (1.00 ± 0.10) and B@CuNi (1.125 ± 0.277). The Cu/Ni ratio obtained for B@CuNi accounts for the equimolar impregnation of olive pits by metal ions.

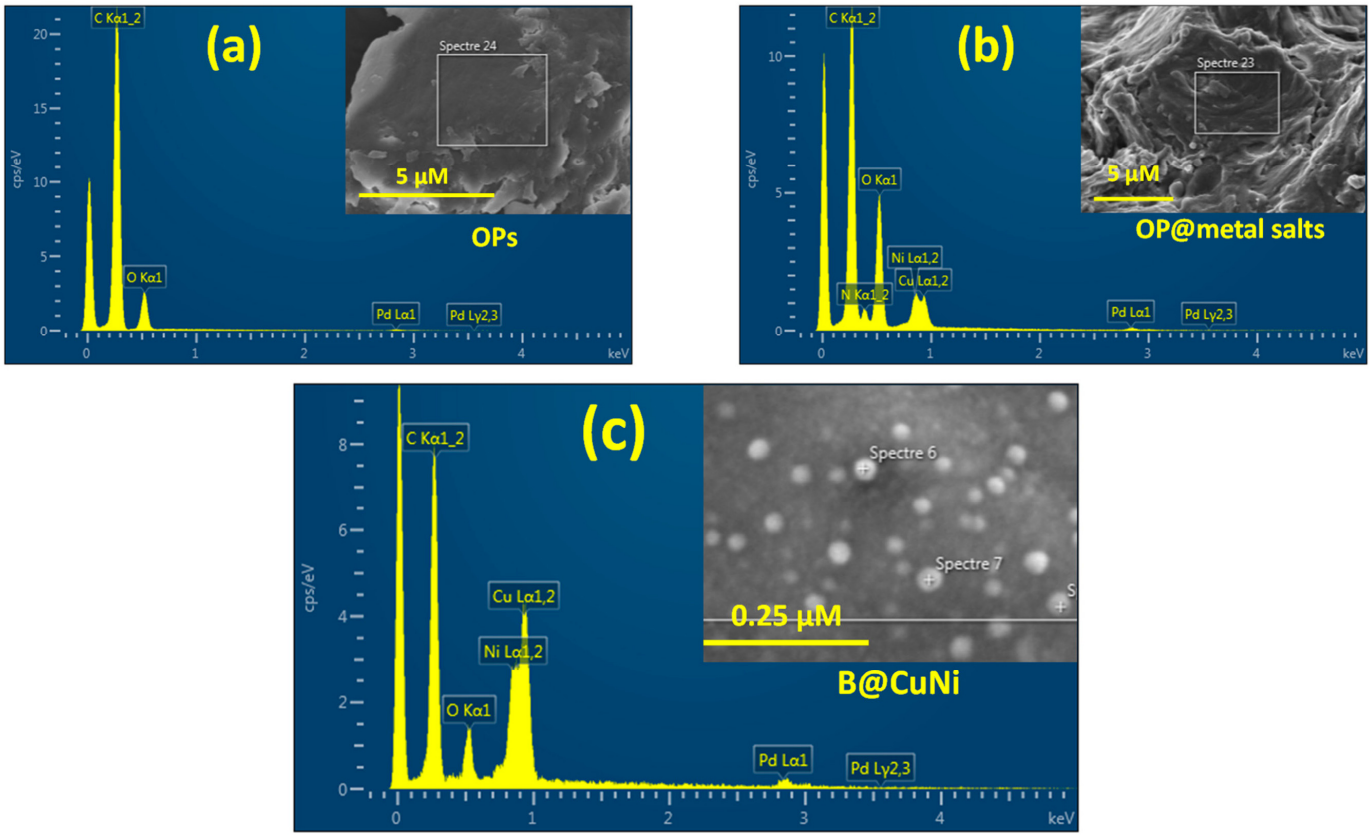

Figure 3. *Cont.*

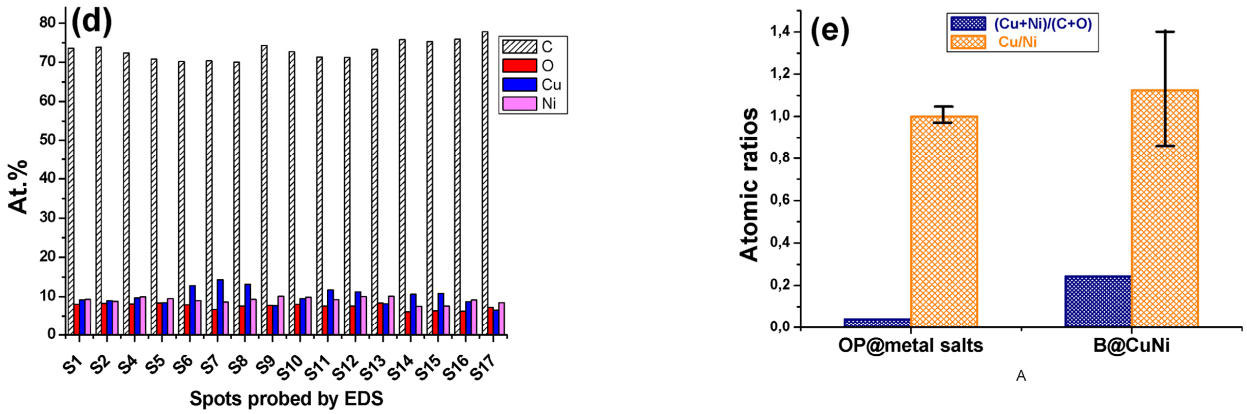

Figure 3. EDX spectra of (**a**) olive pit powder particles, OPs; (**b**) OPs impregnated with metal salts (copper and nickel nitrates), and (**c**) B@CuNi. SEM images show spots probed for the acquisition of EDX spectra. EDX quantification: (**d**) elemental analysis of C, O, Cu and Ni detected at 15 spots of B@CuNi surface; and (**e**) (Cu+Ni)/(C+O) and Cu/Ni atomic ratios averaged over 15 spots.

3.3. Phase Analysis

The prepared catalysts were analysed using both XRD and Raman to identify the nature of the metal and carbon contents, respectively. Figure 4 displays XRD patterns of B@CuNi and of the reference materials Biochar and B@Ni. Those of B@Ni and B@Cu (not shown) correspond very well to the structures of nickel and copper-face-centered cubic metals (ICDD n°98-004-1508 and 98-005-2256), respectively. The XRD pattern of B@CuNi exhibits the same type of diffraction lines but at 2θ positions located between those of pure Cu and pure Ni phases, suggesting that the biochar serves as a support of a $Ni_{1-x}Cu_x$ metallic solid solution. This is a strong supporting evidence that copper and nickel were alloyed during the one-step pyrolysis process. Moreover, it is noteworthy that all peaks are broadened, which is in line with the production of small crystals that were imaged by SEM (see Figure 2b,c). However, as the technique probes the bulk, no surface oxidation of the nanocatalysts was detected. This would best be accomplished using the more specific technique X-ray photoelectron spectroscopy (XPS). Indeed, elsewhere, surface oxidation of nickel [21], copper [21,22] and iron [14] loaded on biochar was detected, as well as the partial oxidation of palladium nanoparticles loaded on organo-functionalized mesoporous silica [23].

The formation of metallic Ni and CuNi particles was also confirmed by measuring the variation in the sample magnetization M as a function of the magnetic field H at room temperature. Indeed, by cycling the magnetic field H between −20.0 and +20.0 kOe, typical soft ferromagnet hysteresis loops with zero remanence and zero coercivity [24] were recorded on both B@CuNi and B@Ni samples (Figure 5). This feature must be underlined since it accounts for the ability of the designed catalysts to be reversibly attracted by an external magnetic field, making their recovery and reuse easy to achieve. Interestingly, as the copper alloyed nickel particles are usually less magnetic than the pure nickel ones, it may be noticed on the recorded M(H) plots that the saturation magnetization of B@Ni is much more quickly reached than that of B@CuNi.

To complete these structural characterizations, Raman spectroscopy was carried out on the prepared sample, with a special emphasis on their carbon signature. The spectrum recorded in the 1000–2000 cm^{-1} energy region for the metal-free Biochar is shown in Figure 6 to illustrate this purpose. It is fitted with five components assigned to S (1262 cm^{-1}; sp^2-sp^3), D (1380 cm^{-1}; sp^2, C-C between aromatic cycles and highly ordered carbon material), V (1506 cm^{-1}; sp^2-sp^3, amorphous carbon structures), G (1596 cm^{-1}; graphite, sp^2) and G_L (1696 cm^{-1}; sp^2, C=O) [25,26]. Particularly, the D and G bands are assigned to disordered and ideal graphitic lattice, respectively. The D/G peak height and area ratios equal 0.66 and 0.87, respectively. The spectrum indicates, therefore, the presence of C

sp^2 atoms but no excess of amorphous sp^3 hydrocarbons. It is noteworthy that the D/G ratio, referring to the degree of defects in the carbon material, is much lower than those reported for hydrothermally synthesized graphene quantum dots [27]. This is also lower than the values reported for pruning wastes of apple trees post-treated at 400 °C (D/G height ratio ~ 0.72) [28], ferrate-activated porous biochar prepared at 900 °C (D/G height ratio = 1.07) [29], and (D/G height ratio = 1.14) [30]. This is important when considering the low pyrolysis temperature and high yield we have obtained, as well as the relatively higher graphitization.

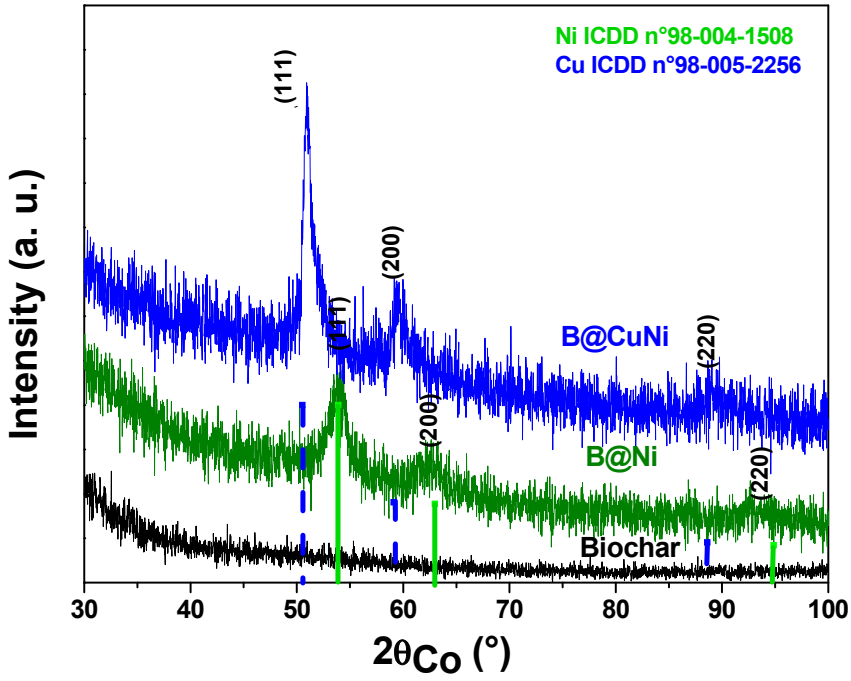

Figure 4. XRD-patterns of B@Ni and B@CuNi samples compared to that of free biochar. The tabulated peak positions of bulk Ni (ICDD n°98-004-1508) and Cu phases (98-005-2256) are given for information.

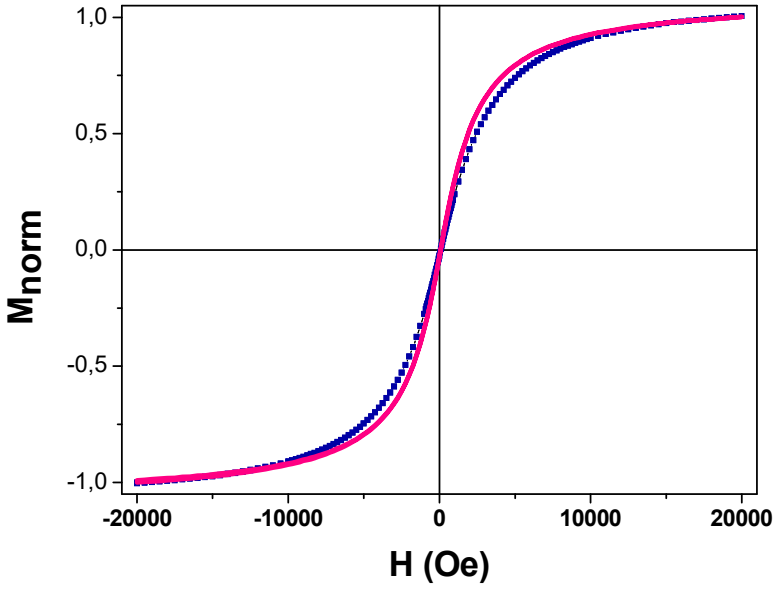

Figure 5. Variation in the normalized magnetization as a function of the magnetic field at room temperature on B@Ni (—) and B@CuNi (■).

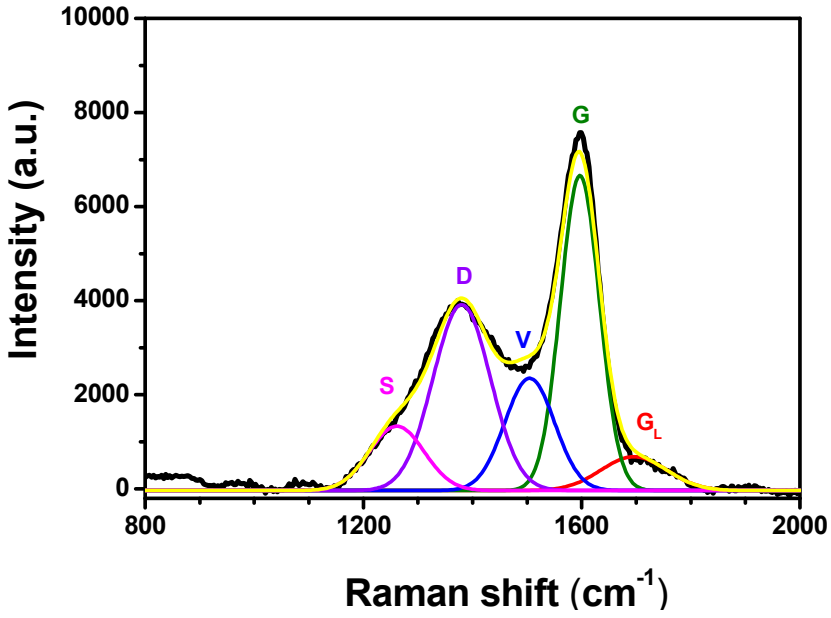

Figure 6. Peak-fitted Raman spectrum of olive pit biochar.

3.4. Thermal Stability

Thermogravimetric analysis (TGA) was utilized as a substantial technique to monitor the thermal stability of biochar and match it with CuNi-decorated biochar. For comparison, we have also plotted the thermograms of B@Cu and B@Ni prepared with single metal ion nitrate. The sequence of residual weight % at a high temperature is Biochar < B@Ni < B@Cu < B@CuNi. This is a logical sequence as, under air, biochar is burnt out, whereas, with nickel, the final biochar is loaded with metallic nickel, which converts to NiO. Copper converts to CuO, and, as both copper and nickel nitrates were impregnated at an equal number of moles per gram of biomass, it is logical to obtain a slightly higher weight % for B@Cu compared to B@Ni. With an increased final number of moles per gram of biochar (see Table 1), biochar burns out, but not the CuNi alloy, which converts to oxides, hence the higher weight % for B@CuNi (lower weight loss). In the literature, carbon@Cu and carbon@Ni prepared by the annealing of the corresponding metal organic frameworks showed only a slight decrease in weight loss because TGA was conducted under an inert atmosphere [20]. In contrast, biochar loaded with a copper complex catalyst exhibited substantial weight loss under air, with a steady state reached at around 500 °C and a final 50% weight [31]. As far as the nickel–biochar-based magnetic catalyst is concerned, a weight loss of 49.8% was reported at 800 °C, presumably under air, but this was not specified [32].

Returning to the main hybrid B@CuNi and reference material Biochar, both samples show a comparable thermal stability behaviour until reaching 240 °C for steady samples withstanding temperature, as shown in Figure 7. Thermogravimetric analysis was carried out under air. A slight increase in the weight of the pristine biochar sample is observed at 280 °C; this is correlated with the oxidation of both biochar and the metal alloy. It might have influenced the biochar specimen and led to a slight increase in its weight %. At higher temperatures, biochar started to decompose at 330–340 °C until reaching 500 °C.

For B@CuNi, a plateau region was reached and corresponds to 42% residual weight of the original sample. The sample retained its thermal stability up to 270–280 °C, then a decomposition step occurred at elevated temperatures to reach a steady state at 455 °C with a residual weight of 45% of the original weight, higher than that of biochar due to loaded metallic nanoparticles [20].

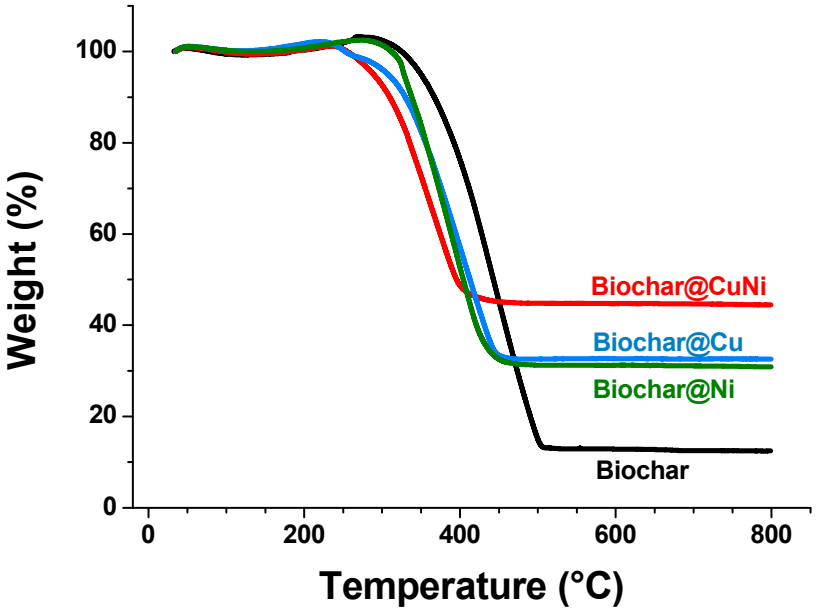

Figure 7. TGA plots recorded under air for biochar and B@CuNi.

From a quantitative viewpoint, the thermograms were obtained under air, which suggests the formation of CuO and NiO, and the weight % differences between pristine and decorated biochar should account for the oxides. B@Cu has a residual weight of 32.6%, and that of biochar is 12.5%. The difference of 20.1% accounts for CuO, which is 0.201 g CuO for 1 g of hybrid biochar B@C, which corresponds to 2.53 mmol Cu per gram of hybrid biochar. This matches the value of 2.489 mmol/g reported in Table 1, corresponding to an error of 1.6%. With the same reasoning, and by subtracting the residual mass of biochar from that of B@Ni, one obtains 2.45 mmol nickel per gram of hybrid biochar, which is 6% less than the value of 2.608 mmol nickel/g B@Ni. Finally, concerning B@CuNi and assuming the initial exact number of moles of nickel and copper nitrates (they differ by only 1%, see Table 1), the weight % difference with biochar is 44.5−12.5 = 32%, i.e., 0.32 g of the NiO/CuO mixture (for Ni/Cu equimolar ratio) per 1 g of hybrid biochar. Assuming a hypothetical oxide $CuNiO_2$ (molar mass = 154.2 g), one would receive 4.15 mmol of copper–nickel mixture, which is 25% less than the total number of moles compared to the expected value reported in Table 1 (5.521 mmol/g). This apparent discrepancy could be due to the incomplete oxidation of larger nanoparticles and possible segregation of one of the metals to the surface of the alloy nanoparticles [33]. This hypothesis requires a full investigation that is beyond the scope of this paper.

3.5. Potential Application: Proof of Concept of Heterogeneous Catalyzed Degradation of Methyl Orange Dye

Dye removal can be achieved through various routes comprising adsorption [34], filtration [35] or catalyzed degradation [36,37]. Here, we focus on the catalyzed degradation of MO in aqueous solution in order to assess the catalytic activity of the actual CuNi-decorated biochar. This process was carried out in the presence of $NaBH_4$ as a reducing agent. Upon starting at time = 0 s, the investigated samples did not show any significant changes in the color of the tested vials, as illustrated in the upper row in Figure 8a. After 30 min, the color of the solution loaded with decorated biochar turned colorless, referring to decomposed MO (Figure 8b). The UV-vis spectra of MO with different reactants in the presence and absence of the decorated biochar are illustrated in Figure 8c. Starting with the spectrum showing peaks with the highest intensity among the explored samples, MO displays a typical intense peak at 464 nm, accompanied by a lower one at 270 nm. The first peak can be correlated with the conjugation of electron donor N=N bond. Meanwhile, the latter peak is related to aromatic pi-pi* transition [38]. After diluting MO with deionized

water, the same behaviour for absorbance bands arose but with lower peak intensities. This may be related to the dilution effect resulting from introducing water to the previously tested MO aqueous solution. The dilution step was implemented to confirm the presence of MO in the solution even at a lower concentration with weaker absorption bands. Upon investigating the samples of MO with either CuNi-decorated biochar or $NaBH_4$ separately, the absorption peaks showed neither significant changes nor shifts. Upon testing MO with B@CuNi and $NaBH_4$, the solution became transparent; this attests to the degradation process of MO. The previously mentioned peaks vanished and new bands appeared at 245 and 248 nm. Accordingly, a cleavage of the –N=N- bond took place to generate the -NH_2 group, hence newly formed species, namely, sulfanilic acid and p-amino dimethylaniline, respectively [39,40] exist. It is noteworthy that no centrifugation was required to split the biochar and the supernatant; the latter was sedimented easily using a magnet, which facilitated sampling of the supernatant for UV-vis analysis.

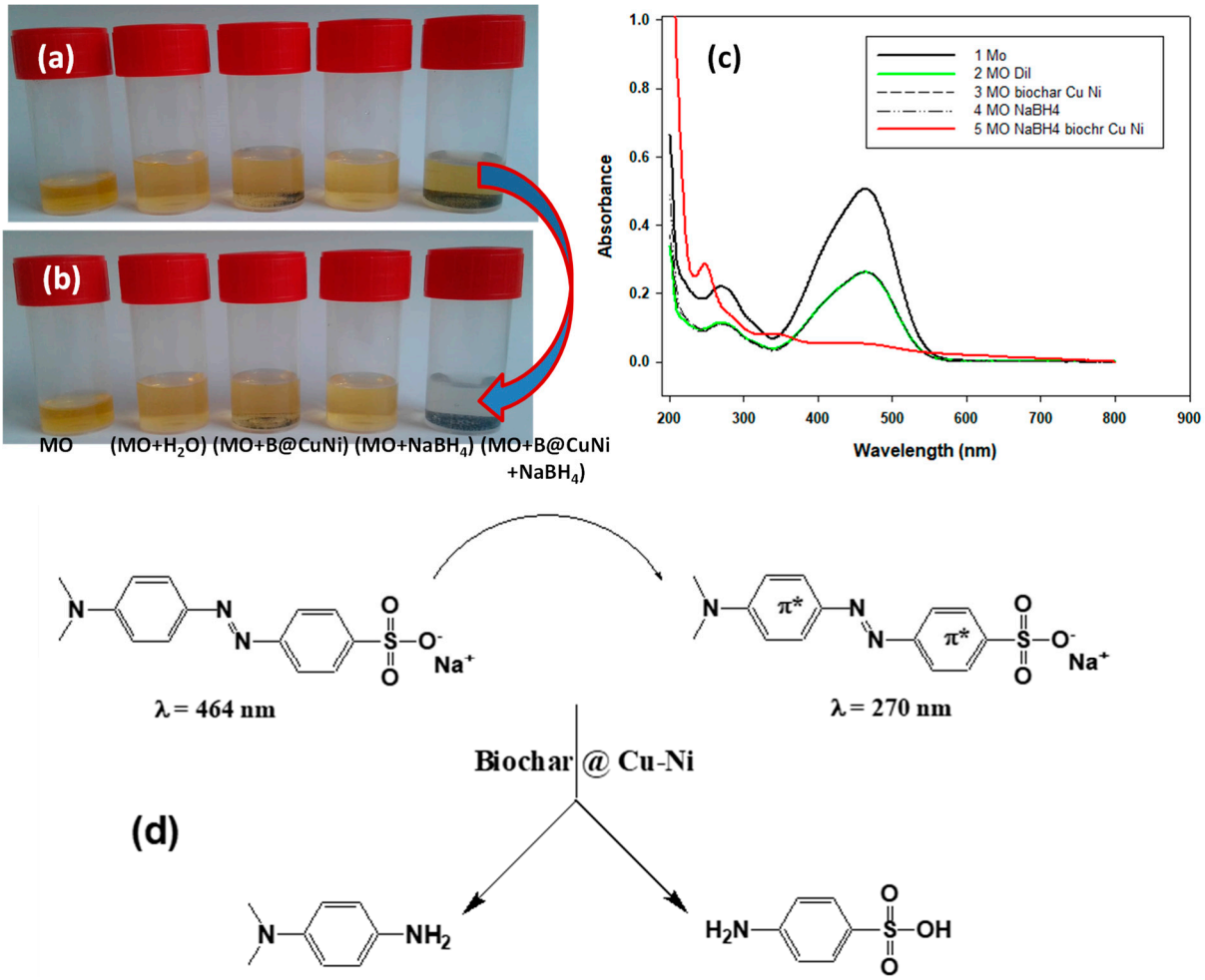

Figure 8. (**a**,**b**) Digital photographs and (**c**) UV-vis spectra for MO vials before and after catalytic reaction. (**d**) A proposed scheme for MO before and after the catalytic degradation with decorated CuNi-biochar.

These preliminary results are encouraging, as the test dye aqueous solution containing ~0.24 µmol MO was discolored in less than 30 min using ~5.5 µmol of alloyed Cu and Ni metals, but the turnover number should be limited to the copper and nickel atoms present at the surface of the bimetallic nanoparticles, thus resulting in a higher TON value. The recovered B@CuNi hybrid catalyst allowed for catalyzing the discoloration of a new, freshly prepared MO solution. This is due to the presence of NBH_4, which could reduce NiO and CuO if they were ever present at the surface of B@CuNi.

To finish, we are presently testing new processes for making biochar@CuNi that permit a faster discoloration of MO solutions (within 1–10 min). The new studies need to be double-checked and confirmed prior to future publication.

4. Conclusions

We have composed a boosted biochar derived from an agrowaste: olive pit (OP) powder. Metallic salts of hydrated nickel and/or copper nitrate(s), as precursors, were mixed with OP, followed by pyrolysis, in one step, at 400 °C to generate biochar@CuNi (B@CuNi). The resulting biochar was characterized by SEM to show a homogenous surface with well-distributed CuNi nanoparticles on the surface of the biochar. EDX and XRD asserted the formation of CuNi nanoparticles as a metallic alloy decorating the biochar. Magnetization experiments accounted for the presence of nickel and demonstrated that nanocatalyst-decorated biochars behave as ferromagnets. B@CuNi showed a high catalytic performance in the decomposition of methyl orange (MO) dye.

The significance of this work lies in the valorization of agrowaste in general and the production of an enhanced biochar decorated with bimetallic nanocatalyst (CuNi) in a facile process in particular. This strategy of making nanocatlyst-doped biochar opens new avenues for water treatment and, therefore, attempts to elegantly contribute to environmental remediation, and thus to address UN Sustainable Development Goal 6 pertaining to clean water and sanitation.

Supplementary Materials: The following are available online at https://www.mdpi.com/article/10.3390/app11188513/s1, Video S1: Attraction of Biochar@CuNi by a magnet.

Author Contributions: Conceptualization (M.M.C. and A.M.K.); Methodology (M.M.C., A.M.K., S.B.); Validation (A.M.K., L.M., R.P., S.B., K.J., S.A., M.J. and M.M.C.); Formal Analysis and Investigation (A.M.K., L.M., R.P., S.B., K.J., S.A., M.J. and M.M.C.); Writing—Original Draft (M.M.C. and A.M.K.); Writing—Review & Editing (A.M.K., L.M., R.P., S.B., K.J., S.A., M.J. and M.M.C.); Resources (M.M.C., L.M., S.B., R.P., S.A.); Supervision (M.M.C.); Funding acquisition (A.M.K., M.M.C.). All authors have read and agreed to the published version of the manuscript.

Funding: A.M.K. and M.M.C. would like to thank both the French and Egyptian Governments for funding AMK's contribution through a fellowship granted by the French Embassy in Egypt (Institut Francais d'Egypte) and Science and Technology Development Fund (STDF)-Egypt, Project number (42248).

Institutional Review Board Statement: Not applicable.

Informed Consent Statement: Not applicable.

Data Availability Statement: Original data available on request. They are not archived in any repository.

Acknowledgments: Stépahnie Lau-Truong is acknowledged for Raman analysis.

Conflicts of Interest: The authors declare no conflict of interest.

References

1. Adeniyi, A.G.; Ighalo, J.O.; Onifade, D.V. Biochar from the Thermochemical Conversion of Orange (*Citrus sinensis*) Peel and Albedo: Product Quality and Potential Applications. *Chem. Afr.* **2020**, *3*, 439–448. [CrossRef]
2. Azeem, M.; Hassan, T.U.; Tahir, M.I.; Ali, A.; Jeyasundar, P.G.S.A.; Hussain, Q.; Bashir, S.; Mehmood, S.; Zhang, Z. Tea leaves biochar as a carrier of Bacillus cereus improves the soil function and crop productivity. *Appl. Soil Ecol.* **2021**, *157*, 103732. [CrossRef]
3. Zubair, M.; Mu'azu, N.D.; Jarrah, N.; Blaisi, N.I.; Aziz, H.A.; AAl-Harthi, M. Adsorption Behavior and Mechanism of Methylene Blue, Crystal Violet, Eriochrome Black T, and Methyl Orange Dyes onto Biochar-Derived Date Palm Fronds Waste Produced at Different Pyrolysis Conditions. *Water Air Soil Pollut.* **2020**, *231*, 240. [CrossRef]
4. Bagheri, A.; Abu-Danso, E.; Iqbal, J.; Bhatnagar, A. Modified biochar from Moringa seed powder for the removal of diclofenac from aqueous solution. *Bhatnagar Environ. Sci. Pollut. Res.* **2020**, *27*, 7318–7327. [CrossRef]
5. Sun, X.; Shan, R.; Li, X.; Pan, J.; Liu, X.; Deng, R.; Song, J. Characterization of 60 types of Chinese biomass waste and resultant biochars in terms of their candidacy for soil application. *Gcb Bioenergy* **2017**, *9*, 1423–1435. [CrossRef]

6. Tripathi, M.; Sahu, J.N.; Ganesan, P. Effect of process parameters on production of biochar from biomass waste through pyrolysis: A review. *Renew. Sustain. Energy Rev.* **2016**, *55*, 467–481. [CrossRef]
7. Luong, D.X.; Bets, K.V.; Algozeeb, W.A.; Stanford, M.G.; Kittrell, C.; Chen, W.; Salvatierra, R.V.; Ren, M.; McHugh, E.A.; Advincula, P.A. Gram-scale bottom-up flash graphene synthesis. *Nature* **2020**, *577*, 647–651. [CrossRef] [PubMed]
8. Lopes, R.P.; Astruc, D. Biochar as a support for nanocatalysts and other reagents: Recent advances and applications. *Coord. Chem. Rev.* **2021**, *426*, 213585. [CrossRef]
9. Shen, Y.; Zhao, P.; Shao, Q.; Takahashi, F.; Yoshikawa, K. In situ catalytic conversion of tar using rice husk char/ash supported nickel–iron catalysts for biomass pyrolytic gasification combined with the mixing-simulation in fluidized-bed gasifier. *Appl. Energy* **2015**, *160*, 808–819. [CrossRef]
10. Tan, G.; Wu, Y.; Liu, Y.; Xiao, D. Removal of Pb(II) ions from aqueous solution by manganese oxide coated rice straw biochar-A low-cost and highly effective sorbent. *J. Taiwan Inst. Chem. Eng.* **2018**, *84*, 85–92. [CrossRef]
11. Guo, F.; Peng, K.; Liang, S.; Jia, X.; Jiang, X.; Qian, L. One-step synthesis of biomass activated char supported copper nanoparticles for catalytic cracking of biomass primary tar. *Energy* **2019**, *180*, 584–593. [CrossRef]
12. Ge, X.; Ge, M.; Chen, X.; Qian, C.; Liu, X.; Zhou, S. Facile synthesis of hydrochar supported copper nanocatalyst for Ullmann C-N coupling reaction in water. *Mol. Catal.* **2020**, *484*, 110726. [CrossRef]
13. Yeşiltepe, S.; Buğdaycı, M.; Yücel, O.; Şeşen, M.K. Recycling of Alkaline Batteries via a Carbothermal Reduction Process. *Batteries* **2019**, *5*, 35. [CrossRef]
14. Tamborrino, V.; Costamagna, G.; Bartoli, M.; Rovere, M.; Jagdale, P.; Lavagna, L.; Ginepro, M.; Tagliaferro, A. Catalytic oxidative desulphurization of pyrolytic oils to fuels over different waste derived carbon-based catalysts. *Fuel* **2021**, *296*, 120693. [CrossRef]
15. Khemakhem, M.; Jaziri, M. Composites based on (ethylene–propylene) copolymer and olive solid waste: Rheological, thermal, mechanical, and morphological behaviors. *Polym. Eng. Sci.* **2016**, *56*, 27–35. [CrossRef]
16. Khalil, A.M.; El-Nemr, K.F.; Hassan, M.L. Acrylate-modified gamma-irradiated olive stones waste as a filler for acrylonitrile butadiene rubber/devulcanized rubber composites. *J. Polym. Res.* **2019**, *26*, 249. [CrossRef]
17. Belbekhouche, S.; Kebe, S.I.; Mahouche-Chergui, S.; Guerrouache, M.; Carbonnier, B.; Jaziri, M.; Chehimi, M.M. Aryl diazonium-modified olive waste: A low cost support for the immobilization of nanocatalysts. *Coll. Surf. A Physicochem. Eng. Asp.* **2017**, *529*, 541–549. [CrossRef]
18. Fernández-Uclés, D.; Elfkih, S.; Mozas-Moral, A.; Bernal-Jurado, E.; Medina-Viruel, M.J.; Abdallah, S.B. Economic Efficiency in the Tunisian Olive Oil Sector. *Agriculture* **2020**, *10*, 391. [CrossRef]
19. Mirzaei, P. Préparation de Matériaux D'électrode Pour L'élimination et La Valorisation de Polluants Azotés. Ph.D. Thesis, Université Paris Est, Paris, France, 2018. Available online: http://www.theses.fr/2018PESC1106 (accessed on 10 September 2021).
20. Ahsan, M.A.; Jabbari, V.; El-Gendy, A.A.; Curry, M.L.; Noveron, J.C. Ultrafast catalytic reduction of environmental pollutants in water via MOF-derived magnetic Ni and Cu nanoparticles encapsulated in porous carbon. *Appl. Surf. Sci.* **2019**, *497*, 143608. [CrossRef]
21. Zhu, C.; Wang, H.; Li, H.; Cai, B.; Lv, W.; Cai, C.; Wang, C.; Yan, L.; Liu, Q.; Ma, L. Selective Hydrodeoxygenation of 5-Hydroxymethylfurfural to 2,5-Dimethylfuran over Alloyed Cu−Ni Encapsulated in Biochar Catalysts. *ACS Sustain. Chem. Eng.* **2019**, *7*, 19556–19569. [CrossRef]
22. Liu, W.-J.; Tian, K.; Jiang, H.; Yu, H.-Q. Harvest of Cu NP anchored magnetic carbon materials from Fe/Cu preloaded biomass: Their pyrolysis, characterization, and catalytic activity on aqueous reduction of 4-nitrophenol. *Green Chem.* **2014**, *16*, 4198–4205. [CrossRef]
23. Saad, A.; Vard, C.; Abderrabba, M.; Chehimi, M.M. Triazole/Triazine-Functionalized Mesoporous Silica As a Hybrid Material Support for Palladium Nanocatalyst. *Langmuir* **2017**, *33*, 7137–7146. [CrossRef] [PubMed]
24. Luo, M.; Huang, C.; Chen, F.; Chen, C.; Li, H. Removal of aqueous Cr(VI) using magnetic-gelatin supported on Brassica-straw biochar. *J. Dispers. Sci. Technol.* **2021**, *42*, 1710–1722. [CrossRef]
25. Shao, Y.; Guizani, C.; Grosseau, P.; Chaussy, D.; Beneventi, D. Biocarbons from microfibrillated cellulose/lignosulfonate precursors: A study of electrical conductivity development during slow pyrolysis. *Carbon* **2018**, *129*, 357–366. [CrossRef]
26. Li, X.; Hayashi, J.-I.; Li, C.-Z. Volatilisation and catalytic effects of alkali and alkaline earth metallic species during the pyrolysis and gasification of Victorian brown coal. Part VII. Raman spectroscopic study on the changes in char structure during the catalytic gasification in air. *Fuel* **2006**, *85*, 1509–1517. [CrossRef]
27. Xiao, X.; Chen, B. A Direct Observation of the Fine Aromatic Clusters and Molecular Structures of Biochars. *Environ. Sci. Technol.* **2017**, *51*, 5473–5482. [CrossRef]
28. Kim, D.-G.; Ko, S.-O. Effects of thermal modification of a biochar on persulfate activation and mechanisms of catalytic degradation of a pharmaceutical. *Chem. Eng. J.* **2020**, *399*, 125377. [CrossRef]
29. Tam, N.T.M.; Liu, Y.; Bashir, H.; Yin, Z.; He, Y.; Zhou, X. Efficient Removal of Diclofenac from Aqueous Solution by Potassium Ferrate-Activated Porous Graphitic Biochar: Ambient Condition Influences and Adsorption Mechanism. *Int. J. Environ. Res. Public Health* **2020**, *17*, 291.
30. Endler, L.W.; Wolfart, F.; Mangrich, A.S.; Vidotti, M.; Marchesi, L.F. Facile method to prepare biochar–NiO nanocomposites as a promisor material for electrochemical energy storage devices. *Chem. Pap.* **2020**, *74*, 1471–1476. [CrossRef]
31. Moradi, P.; Hajjami, M.; Tahmasbi, B. Fabricated copper catalyst on biochar nanoparticles for the synthesis of tetrazoles as antimicrobial agents. *Polyhedron* **2020**, *175*, 114169. [CrossRef]

32. Moradi, P.; Hajjami, M. Magnetization of biochar nanoparticles as a novel support for fabrication of organo nickel as a selective, reusable and magnetic nanocatalyst in organic reactions. *New J. Chem.* **2021**, *45*, 2981–2994. [CrossRef]
33. Charan, P.H.K.; Rao, G.R. Synthesis of CuNi and CuNi/SBA-15 by aqueous method at room temperature and their catalytic activity. *Microporous Mesoporous Mater.* **2014**, *200*, 101–109. [CrossRef]
34. Khalil, A.M.; Kenawy, S.H. Hybrid Membranes Based on Clay-Polymer for Removing Methylene Blue from Water. *Acta Chim. Slov.* **2020**, *67*, 96–104. [CrossRef]
35. Abdelhamid, A.E.; El-Sayed, A.A.; Khalil, A.M. Polysulfone nanofiltration membranes enriched with functionalized graphene oxide for dye removal from wastewater. *J. Polym. Eng.* **2020**, *40*, 833–841. [CrossRef]
36. Ait-Touchente, Z.; Khalil, A.M.; Simsek, S.; Boufi, S.; Ferreira, L.F.V.; Vilar, M.R.; Touzani, R.; Chehimi, M.M. Ultrasonic effect on the photocatalytic degradation of Rhodamine 6G (Rh6G) dye by cotton fabrics loaded with TiO_2. *Cellulose* **2020**, *27*, 1085–1097. [CrossRef]
37. Mousli, F.; Khalil, A.M.; Maurel, F.; Kadri, A.; Chehimi, M.M. Mixed oxide-polyaniline composite-coated woven cotton fabrics for the visible light catalyzed degradation of hazardous organic pollutants. *Cellulose* **2020**, *27*, 7823–7846. [CrossRef]
38. Yang, L.; Wang, Q.; Rangel-Mendez, J.R.; Jia, F.; Song, S.; Yang, B. Self-assembly montmorillonite nanosheets supported hierarchical MoS2 as enhanced catalyst toward methyl orange degradation. *Mater. Chem. Phys.* **2020**, *246*, 122829. [CrossRef]
39. Bakhsh, E.M.; Khan, S.A.; Marwani, H.M.; Danish, E.Y.; Asiri, A.M.; Khan, S.B. Performance of cellulose acetate-ferric oxide nanocomposite supported metal catalysts toward the reduction of environmental pollutants. *Int. J. Biol. Macromol.* **2018**, *107*, 668–677. [CrossRef]
40. Sha, Y.; Mathew, I.; Cui, Q.; Clay, M.; Gao, F.; Zhang, X.J.; Gu, Z. Rapid degradation of azo dye methyl orange using hollow cobalt nanoparticles. *Chemosphere* **2016**, *144*, 1530–1535. [CrossRef]